International Journal of Nanomedicine

Dovepress
Taylor & Francis Group

Open Access Full Text Article

ORIGINAL RESEARCH

Exploring Carbon Dot Nanoparticles for Imaging and Cellular Interaction in Triple-Negative Breast Cancer

Mehrnoosh Bahadorani[1], Kerui Wu[2], Jianjun Wei[2], Reza Zadegan[1]

[1]Department of Nanoengineering, Joint School of Nanoscience & Nanoengineering, North Carolina Agriculture and Technical State University, Greensboro, NC, USA; [2]Department of Nanoscience, Joint School of Nanoscience and Nanoengineering (JSNN), University of North Carolina at Greensboro, Greensboro, NC, USA

Correspondence: Reza Zadegan; Jianjun Wei, Email rzadegan@ncat.edu; j_wei@uncg.edu

Introduction: Carbon dot nanoparticles (CNDs) are widely regarded as biocompatible agents for cellular imaging due to their strong fluorescence and ease of synthesis. However, their biological effects remain insufficiently characterized.

Methods: We synthesized carbon nanodots (E-CNDs) using a microwave-assisted method with citric acid and ethylenediamine. Their intracellular distribution and potential impact on triple-negative breast cancer (TNBC) cells were investigated.

Results: After 16 hours of incubation with E-CNDs (up to 0.8 mg/mL), imaging revealed strong perinuclear localization, moderate mitochondrial presence, and no detectable nuclear signal. These observations supported their use in intracellular imaging and motivated further analysis of their biological effects. While CCK-8 assays showed no significant cytotoxicity across concentrations, molecular analysis revealed dose-dependent downregulation of glucose-6-phosphate dehydrogenase (G6PDH) and upregulation of procaspase 3, aligning with increased apoptotic activity detected by Annexin V/PI staining.

Conclusion: These results show that although E-CNDs appear non-toxic by standard viability assays and function effectively as imaging agents, they also trigger measurable molecular and apoptotic responses. This underscores that cell viability alone is insufficient to assume biocompatibility. More detailed molecular and functional assessments are needed to establish reliable safety profiles, which are critical for the safe design and evaluation of nanomaterials in biomedical applications.

Keywords: carbon dot nanoparticles, triple-negative breast cancer, bioimaging, oxidative stress, apoptosis, biocompatibility, nanotoxicology

Introduction

Bioimaging is an indispensable tool in medical and biological research. The development of carbon nanodots (CNDs) through nanotechnology has significantly advanced this field.[1] Given the increasing demand for sensitive and targeted imaging agents, especially in oncology, CNDs have attracted growing interest for cancer diagnostics and therapy. Cancer remains one of the leading causes of death worldwide, responsible for nearly 10 million deaths in 2020, accounting for almost one in six deaths globally.[2] Among the most prevalent types of cancer are breast, lung, colon, rectum, and prostate cancer. Early detection significantly improves treatment outcomes and survival rates.[3] Nanotechnology has opened promising avenues for tumor-targeted imaging, where nanoprobes can accumulate in tumor tissues through the enhanced permeability and retention (EPR) effect[4,5] or via active targeting using specific surface ligands.[6]

CNDs, known for their unique luminescent properties such as chirality,[7] room temperature phosphorescence,[8] multiple photoluminescence,[9] and thermally induced delayed fluorescence,[10] have become prime candidates for bioimaging applications.[5,11] Their excellent photostability, tunable photoluminescence, and ability to traverse biological barriers, including the blood-brain barrier,[12] provide distinct advantages over traditional imaging probes[13] and make them ideal for real-time in vivo and tissue imaging with deep penetration, facilitating long-term monitoring of biological processes.[5]

Received: 3 June 2025
Accepted: 14 October 2025
Published: 9 December 2025

Graphical Abstract

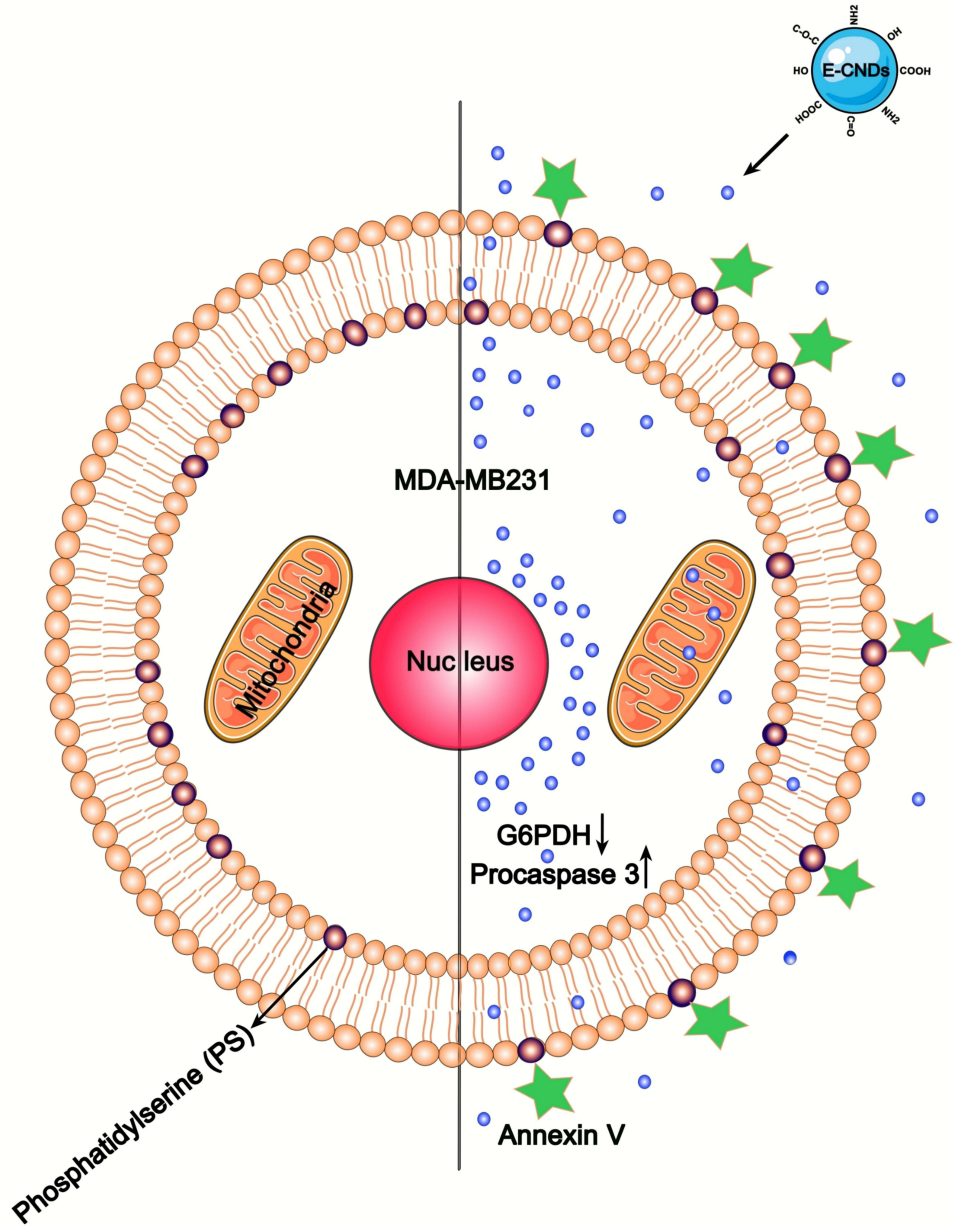

Beyond imaging, CNDs also demonstrate potential for broader cancer-related applications, including drug delivery, photothermal therapy, and photodynamic therapy.[14] These nanodots typically enter cells through passive endocytosis and stain the cell membrane and perinuclear space.[15] However, cell types can affect the uptake and exocytosis of the CNDs.[16] Achieving precise organelle targeting, including the nucleus, requires specific ligands.[15] For instance, the surface modifications of the CNDs with L-cysteine target the Golgi apparatus.[17] Recent research has highlighted the various behaviors of CNDs. As Shen et al noted in their review, CNDs can exhibit uniform permeation across many types of cells or distinct accumulation within tumor tissues, attributed to the enhanced permeability and retention (EPR) effect.[5]

While their versatility and ability to enter cells make CNDs promising tools in biomedical applications, growing evidence suggests that their safety profile should be assessed more deeply. They are often described as biocompatible due to their carbon-based composition.[18–20] However, recent studies have raised concerns about the biological effects of CNDs. Liu et al reported that these nanoparticles degrade upon light exposure, resulting in toxic byproducts that significantly increase cytotoxicity in human cells.[21] Their study highlighted that although CNDs may appear stable and non-toxic under dark conditions, illumination can trigger chemical changes that compromise cell viability, emphasizing the importance of evaluating nanoparticle stability under biologically relevant conditions.

Separately, a study by another group[22] investigated the biocompatibility of CNDs in live animal models using zebrafish due to their genetic similarity to humans, transparency during early development, and rapid reproduction rate. These features make zebrafish an ideal model for assessing nanomaterial toxicity and underscore the importance of thoroughly evaluating CNDs interactions with biological systems before clinical application. In their study, CND exposure at concentrations above 200 μg/mL was associated with signs of embryonic toxicity, including yolk and pericardial sac edema, growth delays, spinal cord deformities, and increased mortality. Additionally, higher concentrations were linked to reductions in dopamine levels, altered locomotor behavior, and histopathological changes in critical organs such as the brain, heart, liver, and gills. These effects may involve oxidative stress and apoptosis mechanisms.[22]

In addition, a recent in vivo study in Drosophila melanogaster examined the safety of carbon dots derived from Withania coagulans. While the CDs were applied for bioimaging, certain modified forms, particularly cysteamine-functionalized CDs, caused neurological, developmental, and morphological abnormalities, including abnormal behavior. These findings emphasize that relying only on cell viability assays may overlook important biological effects, and that comprehensive toxicity evaluation is necessary to assess the safety of carbon dots for biomedical use.[23]

These findings show that while in vitro assays such as CCK-8 or Alamar blue often report carbon dots as non-toxic, in vivo studies in zebrafish and fruit flies have revealed developmental, and neurological abnormalities. This indicates that cell viability alone does not provide a full picture of biological safety and that more detailed molecular and functional evaluations are required before drawing reliable conclusions about their biocompatibility.

In this study, we used non-functionalized carbon nanodots synthesized from citric acid and ethylenediamine (E-CNDs) as a model. Our aim was to test whether cell viability results are sufficient to judge biocompatibility, or whether deeper assessment reveals additional biological responses. Using MDA-MB-231 triple-negative breast cancer cells as a representative model, we examined subcellular localization, changes in the expression of glucose-6-phosphate dehydrogenase (G6PDH) and procaspase-3, and apoptosis by Annexin V/PI staining. This approach allowed us to evaluate how E-CNDs interact with cells beyond simple viability testing.

Methods

This section details the experimental procedures employed in this study. First, the synthesis and characterization of E-CNDs are described. This is followed by the cell culture protocol used to maintain and treat MDA-MB-231 triple-negative breast cancer cells. The subsequent sections explain the techniques used to evaluate the intracellular localization of E-CNDs through confocal microscopy. Finally, the methodology for assessing gene expression changes related to oxidative stress and apoptosis using RNA extraction and quantitative PCR is presented, followed by the flow cytometry-based apoptotic assay.

Synthesis and Characterization of E-CNDs

Following the synthesis protocol by Arvapalli et al (2020), E-CNDs were synthesized using a microwave-assisted procedure. In a nutshell, 960 mg of citric acid (Sigma Aldrich, Germany) was combined with 1 mL ethylenediamine (Sigma Aldrich, Germany) and 1 mL deionized water and pyrolyzed in a microwave synthesizer (CEM Discover 2.0 Microwave Synthesizer) under reflux for 18 minutes at 150 °C and 300 W power to create E-CNDs. The resulting brown foamy solution was dissolved in 5 mL of deionized water and dialyzed through an MWCO 1000 membrane (Sigma Aldrich, Germany) in deionized water for 48 hours. The cooled reactant mixture was centrifuged at 3500 rpm for 20 min to remove aggregated particles. Finally, the E-CNDs solutions were freeze-dried using a Labconco Free Zone 6 Freeze Dryer.[24]

The structural and optical properties of E-CNDs were assessed using different techniques. The size of E-CNDs was evaluated using Atomic Force Microscopy (AFM). A 0.002 mg/mL solution of E-CNDs in deionized water was sonicated for 20 minutes, drop-cast onto a mica substrate, and allowed to dry. The size of the particles was then measured using AFM (Asylum MFP-3D Origin+) based on the height profiles. The hydrodynamic size of E-CNDs was measured in cell culture medium at a concentration of 0.005 mg/mL following 20 minutes of ice-bath sonication using a Zetasizer Ultra (Malvern). The functional groups on the E-CNDs surface were analyzed using Fourier Transform Infrared Spectroscopy (FTIR; Varian 670). Fluorescence spectra of E-CNDs were recorded using a FluoroMax-4 fluorometer (Horiba) at excitation wavelengths ranging from 280 to 400 nm (280, 300, 320, 340, 360, 380, and 400 nm). The surface charge of E-CNDs (0.005 mg/mL) was measured using dynamic light scattering (DLS) with a Zetasizer (Malvern ZEN3600). The excitation peak of E-CNDs was determined using UV-Vis spectrophotometry (Cary 60 UV-Vis Spectrophotometer).

Cell Culture Procedure

The human triple-negative breast cancer cell line MDA-MB-231 (ATCC, HTB 26) was used in this study. Cells were cultured in high-glucose DMEM (Gibco™, 11965126, Thermo Fisher) supplemented with 10% fetal bovine serum (FBS; A5256701, Thermo Fisher). After a 24-hour attachment period, cells underwent stepwise serum deprivation, incubating sequentially in DMEM containing 5%, 2%, and 1% FBS, each for 2 hours. Following serum reduction, cells were washed with prewarmed PBS and incubated with E-CNDs for 16 hours.

We evaluated cell viability at concentrations ranging from 0.1 to 3.2 mg/mL to define a suitable concentration range for E-CNDs treatment. Increased cell detachment and reduced viability were observed at 1.6 and 3.2 mg/mL (Figure S1), and these concentrations were excluded from all subsequent assays.

To evaluate cytotoxicity, we seeded MDA-MB-231 cells at 10,000 cells per well in 96-well black/clear-bottom plates (Thermo Scientific™, 12–566-70) using high-glucose DMEM supplemented with 10% FBS. After 12 hours, cells were washed and treated with 100 µL of E-CNDs at concentrations of 0, 0.1, 0.5, or 0.8 mg/mL in fresh medium. Following 16 hours of incubation, cells were rinsed with PBS and incubated with 10 µL of CCK-8 reagent (Invitrogen, DAL1100) in 90 µL of media for 2 hours. Fluorescence was recorded using a BioTek SYNERGYMX plate reader (Gen5 software) at excitation/emission wavelengths of 560/580 nm. Control wells without CCK-8 were included to correct E-CNDs autofluorescence, and their signal was subtracted from test readings.

E-CNDs Intracellular Tracking

The localization of E-CNDs (0.8 mg/mL) in mitochondria or nuclei was evaluated using Confocal Laser Scanning Microscopy (CLSM). Cells (10,000 per well) were seeded on tissue culture-treated 15-well ibidi slides pre-coated with 0.01% poly-L-lysine (Sigma, 25988–63-0) to promote adherence. After the attachment period, cells were incubated with E-CNDs for 16 hours. Cells were then stained with 100 nM MitoTracker Red (MitoTracker™ Red FM; M22425, Thermo Fisher) for 15 minutes, followed by multiple washes. Live-cell CLSM imaging was performed at 37 °C, 5% CO_2, and controlled humidity to monitor E-CNDs fluorescence (excitation: 360 nm, emission: 470 nm) and MitoTracker Red fluorescence (excitation: 579 nm, emission: 599 nm). Mean fluorescence intensity (MFI) was quantified in Fiji ImageJ by selecting regions exhibiting fluorescence from MitoTracker and E-CNDs, with background subtraction performed using negative controls.[25]

For nuclear localization studies, we incubated the cells with E-CNDs for 16 hours. After incubation, cells were washed with PBS and fixed with 4% paraformaldehyde (J19943.K2, Thermo Scientific) for 10 minutes at room temperature. Following three washes with PBS, the cells were simultaneously permeabilized and stained with a mixture of 0.1% Triton X-100 (85111; ThermoFisher) and 0.3 µg/mL (1.5 mM) Propidium Iodide (PI; P3566; ThermoFisher) for 3 minutes. After additional washing steps, the cells were imaged using CLSM after applying a drop of ibidi Mounting Medium (50001; ibidi) to the samples.

E-CNDs Effects on Oxidative Stress-Related and Proapoptotic RNA Levels

In this experiment, the effects of E-CNDs (0.1 or 0.8 mg/mL) on MDA-MB-231 cells were evaluated by measuring the expression of G6PDH (involved in oxidative stress) and procaspase 3 (a proapoptotic marker). After standard cell culture and overnight attachment, cells were incubated with E-CNDs at 0.1 mg/mL and 0.8 mg/mL in cell media. RNA expression levels were compared to untreated control cells, with normalization to β-Actin as the endogenous reference gene.

Total RNA was extracted using the PureLink™ RNA Mini Kit (12183018A, Thermo Fisher) following the manufacturer's protocol and quantified using a NanoDrop spectrophotometer to assess RNA yield and purity. For cDNA synthesis, 100 ng of total RNA per reaction was reverse-transcribed using the High-Capacity RNA-to-cDNA™ Kit (4387406, Thermo Fisher). The resulting cDNA (final concentration: 10 ng/μL) was then used for quantitative qPCR analysis (ΔΔCt method) on an Applied Biosystems Fast 7500 qPCR instrument.

Forward and reverse primers for β-Actin and G6PDH were selected based on NCBI Reference Sequences NM_001101.5 and NM_001360016.2, respectively, and sourced from a previous study.[26] Procaspase 3 primers were designed based on the NCBI Reference Sequence NM_001354777.2. All probes were designed with a 5-base pair gap between the 3′ end of the forward primer and the 5′ end of the probe. The probe reporter dye was FAM, paired with an ABkFQ quencher at the 3' end (Table 1).

qPCR reactions were performed using TaqMan™ Universal Master Mix II with UNG (4440042, ThermoFisher) with standardized concentrations of 500 nM for both forward and reverse primers and 250 nM for the probe across all comparisons. The thermal cycling conditions included an initial incubation at 50 °C for 2 minutes, enzyme activation at 95 °C for 10 minutes, followed by 40 cycles of denaturation at 95 °C for 15 seconds and annealing/extension at 60 °C for 1 minute using standard ramp rate settings. Finally, the results were analyzed using the $2^{-\Delta\Delta Ct}$ method to determine relative gene expression changes.

Apoptosis Assays

Cells were seeded in 6-well dishes and incubated with either 0.1 or 0.8 mg/mL E-CNDs for 16 hours. Following incubation, cells were stained with Alexa Fluor 488-conjugated Annexin V (V13241; Thermo Fisher) to detect early apoptotic cells and propidium iodide (PI) to identify late apoptotic and necrotic cells. Staining was performed according to the manufacturer's instructions, and samples were analyzed using a Beckman Coulter CytoFLEX Flow Cytometer. Data were processed to quantify early apoptotic (Annexin V+/PI−), late apoptotic/necrotic (Annexin V+/PI+), and necrotic (Annexin V−/PI+) cell populations. The data were analyzed using FlowJo (version 10.10.0, FlowJo LLC, Ashland, OR, USA).

Table 1 PCR Primer and Probe Sequences for G6PDH, Procaspase 3, and β-Actin, with T_a and Product Size

Gene	Sequence	* T_a	Product Size (bp)
β-Actin	Forward: CACCATTGGCAATGAGCGGTTC Reverse: AGGTCTTTGCGGATGTCCACGT Probe: CCCTGAGGCACTCTTCCAGCCTTCCTTCC	58.89	135
G6PDH	Forward: CGAGGCCGTCACCAAGAAC Reverse: GTAGTGGTCGATGCGGTAGA Probe: CGAGTCCTGCATGAGCCAGATAGGCTGG	56	166
Procaspase 3	Forward: GGCGGTTGTAGAAGAGTTTCG Reverse: TCACGGCCTGGGATTTCAAG Probe: CTCGCAGCTCATACCTGTGGCTGTGTATC	58.71	101

Note: * T_a: annealing temperature.

https://doi.org/10.2147/IJN.S544373

Results

This section presents the results of E-CNDs characterization, cellular uptake, gene expression analysis, and apoptotic assays following E-CNDs synthesis and cell incubation.

E-CNDs Characterization

E-CNDs characterization was performed using AFM, FTIR, UV-Vis spectroscopy, fluorescence spectroscopy, and zeta potential analysis.

AFM analysis showed that E-CNDs exhibited particle heights in the sub-nanometer range (Figure 1A and B), with quantitative measurements indicating a mean height of 0.64 ± 0.02 nm (Figure 1C). Dynamic light scattering (DLS)

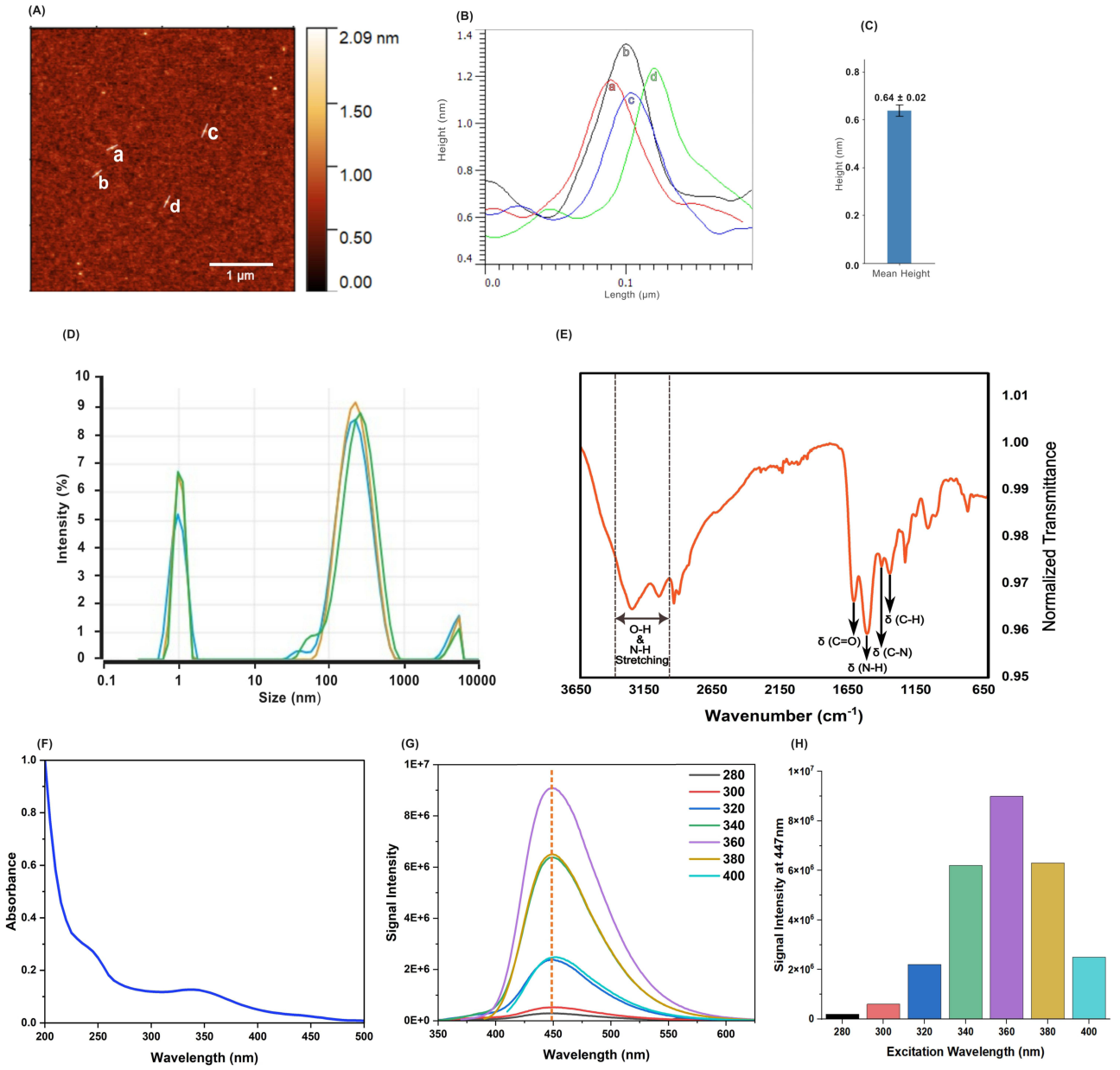

Figure 1 The E-CNDs physicochemical characterization. (**A**) AFM image of E-CNDs deposited on mica. Cross-sections used for height profiling are marked a–d. Scale bar: 1 µm. (**B**) Height profiles corresponding to cross-sections a–d in (**A**), showing particle heights in the nanometer range. (**C**) Mean AFM height of E-CNDs (0.64 ± 0.02 nm). (**D**) DLS analysis revealing two populations: a minor peak at ~1–2 nm and a clustered population at ~239–273 nm. (**E**) FTIR spectrum of E-CNDs. Black arrows indicate the main vibrational peaks (C=O ~1650 cm^{-1}, N–H bending ~1570 cm^{-1}, C–N stretching ~1400 cm^{-1}, C–H bending ~1150 cm^{-1}). The dotted box highlights the O–H and N–H stretching region (3150–3650 cm^{-1}). (**F**) UV–Vis absorption spectrum and (**G**) fluorescence emission spectra of E-CNDs. (**H**) Emission intensity at 447 nm across different excitation wavelengths.

further confirmed this by showing two populations: a peak at ~1–2 nm, in reasonable agreement with AFM measurements, and a clustered population at ~200–270 nm (Figure 1D), with PDI values indicating moderate polydispersity (0.69 ± 0.31). These results suggest that E-CNDs exist as ultrasmall cores together with larger clustered species in suspension, which may enhance photoluminescence via aggregation-induced emission (AIE).[27]

To better understand the organic functional groups on the surface of the E-CNDs, we conducted further analysis using FTIR spectroscopy. In the FTIR spectrum of E-CNDs (Figure 1E), peaks at 1650, 1538, 1432, and 1375 cm^{-1} correspond to C=O, N-H, C-N, and C-H functional groups, respectively. Additionally, bending vibrations of N–H and O–H are observed in the range of 3000 to 3400 cm^{-1}.[24]

The UV-Vis absorption spectrum of E-CNDs (Figure 1F) displays two prominent peaks at 240 nm and 340 nm. The 240 nm peak corresponds to the π–π* transitions of C=C, while the 340 nm peak is associated with n–π* transitions of non-binding orbitals, primarily associated with C=O. Based on the excitation at 340 nm, the location of the E-CNDs has been assessed using the DAPI filter on CLSM.[27]

To characterize the photoluminescent properties of E-CNDs, we recorded their fluorescence emission spectra in deionized water (0.025 mg/mL) under various excitation wavelengths (280–400 nm). The emission intensity increased with excitation up to 360 nm, which produced the strongest signal with a peak emission at 447 nm (Figure 1G), and the relative intensities at this maximum varied across excitation wavelengths (Figure 1H). This strong blue emission highlights the efficient photoluminescence properties of E-CNDs and underscores their suitability for bioimaging applications.

The surface charge of E-CNDs was assessed by measuring their zeta potential using a Zetasizer (Malvern ZEN3600) at a concentration of 0.005 mg/mL. The particles exhibited a negative zeta potential of −16.3 ± 4.91 mV, indicating moderate colloidal stability in aqueous suspension.

Cell Viability Assessment

To evaluate potential cytotoxic effects of E-CNDs, cells were incubated with concentrations of 0.1, 0.5, and 0.8 mg/mL for 16 hours. Across all tested doses, cell viability remained comparable to untreated controls, indicating that E-CNDs did not induce measurable toxicity under these conditions (Figure 2).

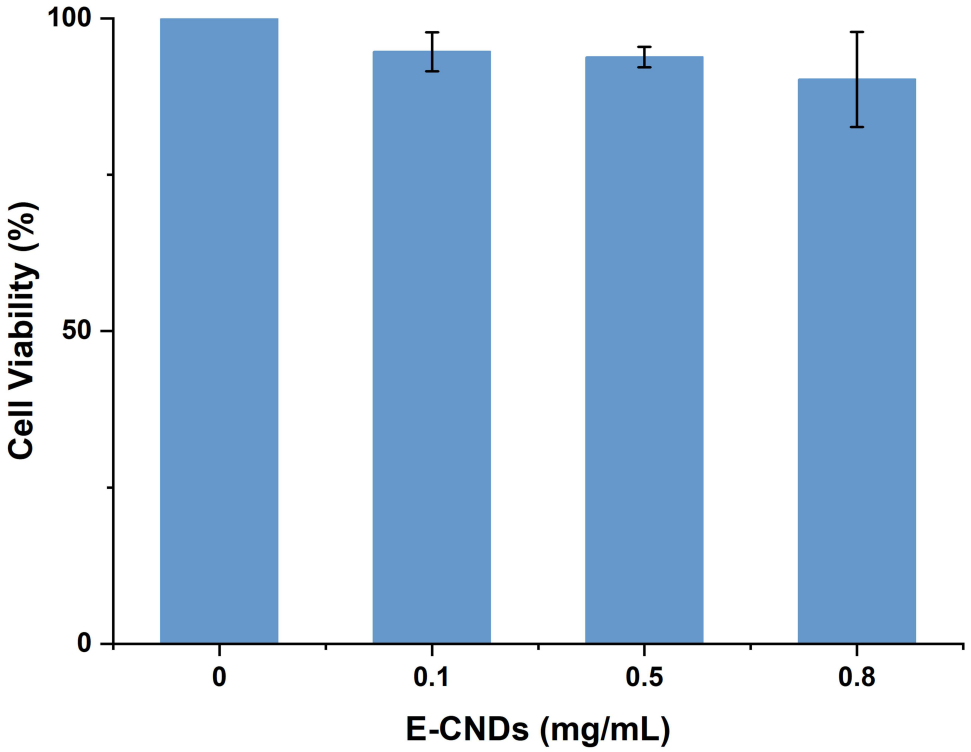

Figure 2 Cell viability of MDA-MB-231 cells treated with E-CNDs. Viability was assessed at 0.1, 0.5, and 0.8 mg/mL E-CNDs compared to untreated controls. Data are shown as mean ± SD from three independent experiments.

https://doi.org/10.2147/IJN.S544373

E-CNDs Cell Internalization and Subcellular Localization

Viability assessments indicated that E-CNDs concentrations up to 0.8 mg/mL had no detectable cytotoxic effects. To determine an appropriate dose for imaging, we tested 0.1, 0.5, and 0.8 mg/mL. Among these, only the 0.8 mg/mL concentration produced a quantifiable fluorescence signal suitable for reliable analysis and was therefore used in all imaging experiments.

To investigate intracellular localization, cells were incubated with 0.8 mg/mL E-CNDs for 16 hours and stained with MitoTracker™ Red FM (M22425, Thermo Fisher) to label mitochondria (Figure 3). E-CNDs exhibited a blue fluorescence signal (Figure 3A), while mitochondria appeared in red (Figure 3B). The merged image (Figure 3C) revealed regions of overlap, with a yellow box marking a representative cell selected for detailed analysis. Figure 3D shows the overlay of both fluorescence channels with the bright-field image, providing morphological context. The distribution of E-CNDs signals colocalized and non-colocalized with mitochondria is quantified in Figure 3E. The mean Mander's coefficient (M1) was approximately 0.49, indicating moderate colocalization, with ~49% of the E-CNDs signal overlapping mitochondrial regions. A 3D fluorescence intensity plot of the highlighted cell (Figure 3F) further demonstrates the spatial relationship between E-CNDs and mitochondria. A broader field of view, including additional cells from the same experiment, is provided in Figure S2.

To further investigate the subcellular localization of E-CNDs, nuclear staining was performed using propidium iodide (PI; P3566, Thermo Fisher) after 16 hours of incubation with E-CNDs. The results showed no evidence of E-CNDs accumulation in the nucleus, as illustrated in Figure 4.

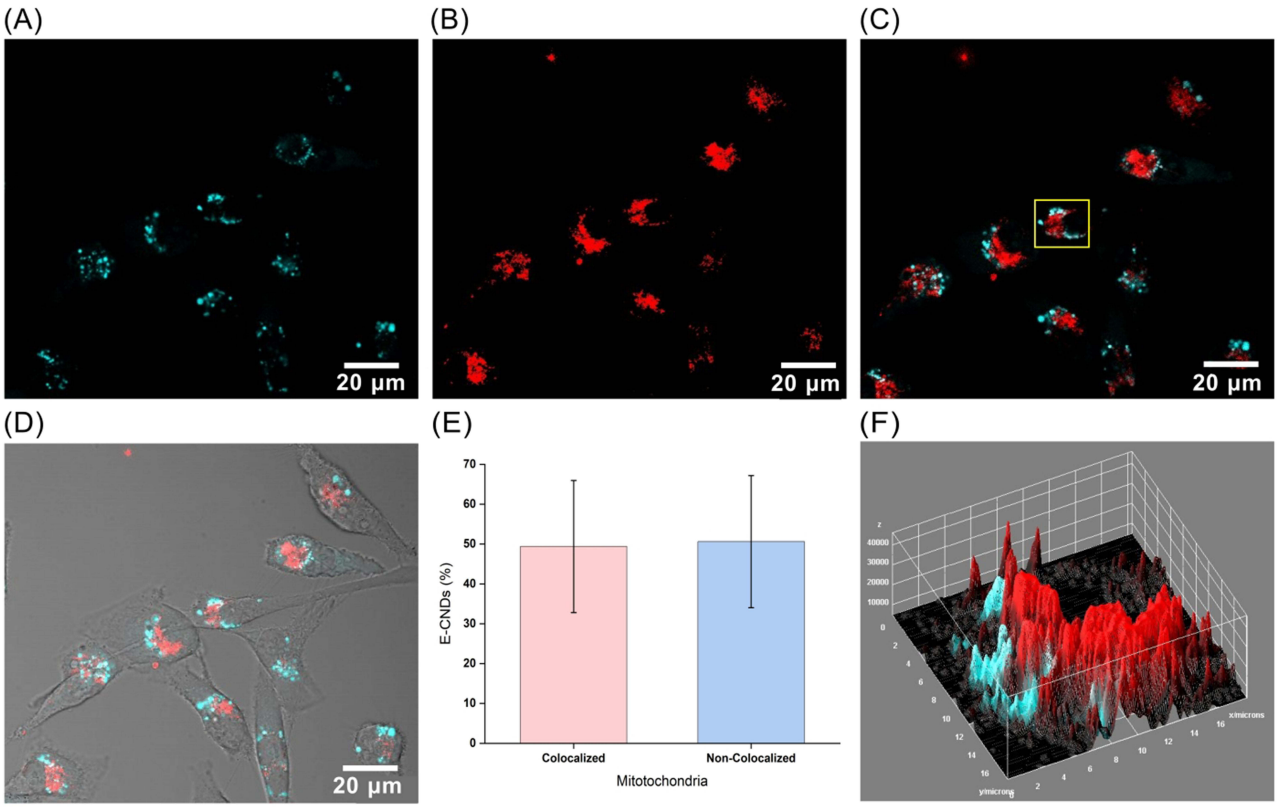

Figure 3 Evaluation of E-CNDs presence in mitochondria of MDA-MB-231 cells. E-CNDs' internalization in the MDA-MB-231 follows 16 hours of incubation with E-CNDs and staining with the Red Mito tracker. The bar shows 20 µm. (**A**) E-CNDs, (**B**) Mito-Tracker Red staining, (**C**) Overlay of (**A** and **B**). (**D**) Overlay of the images with the bright channel. (**E**) Quantification of E-CNDs signal colocalized vs non-colocalized with mitochondria. (**F**) The 3D surface plot of fluorescence intensity from the region highlighted by the yellow box in (**C**) showing the partial overlap of E-CNDs with the mitochondrial signal.

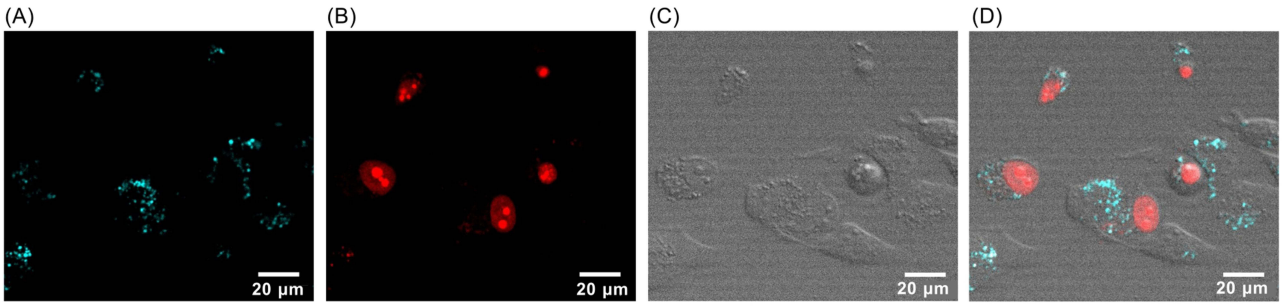

Figure 4 Evaluation of E-CNDs signal in the nucleus of MDA-MB-231 cells. E-CNDs' internalization in the MDA-MB-231 follows 16 hours of incubation with E-CNDs and staining with propidium iodide (PI). The bar shows 20 µm. (**A**) E-CNDs fluorescence, (**B**) Nucleus stained with PI, (**C**) Bright-field image, (**D**) Overlay of all channels.

Relative Expression of Oxidative and Proapoptotic mRNA Using qPCR

To further investigate the intracellular effects of E-CNDs on cellular function, particularly their influence on metabolic and apoptotic pathways, we analyzed the relative mRNA expression of G6PDH and procaspase 3 following 16 hours treatment with 0.1 and 0.8 mg/mL concentrations. These two doses were selected to compare potential dose-dependent responses.

Relative mRNA expression analysis showed that G6PDH was significantly downregulated in both the 0.1 and 0.8 mg/mL E-CNDs-treated groups compared to the control ($p < 0.05$), with about a 20% decrease in expression (Figure 5A). In contrast, procaspase 3 expression (Figure 5B) increased markedly in a dose-dependent manner, showing an approximate 2-fold rise at 0.1 mg/mL and a 3-fold increase at 0.8 mg/mL ($p < 0.001$). The difference in procaspase 3 levels between the two treatment groups was also statistically significant, with higher expression observed at the 0.8 mg/mL concentration ($p < 0.05$).

Proapoptotic Assessment Using Annexin V-PI Kit

Annexin V–PI staining was performed after 16 hours of E-CNDs treatment to evaluate their proapoptotic effects. While the increase in apoptotic cell percentage at 0.8 mg/mL appeared modest, it was statistically significant compared to both the control and 0.1 mg/mL groups ($p < 0.01$). In contrast, no significant difference was observed between the 0.1 mg/mL

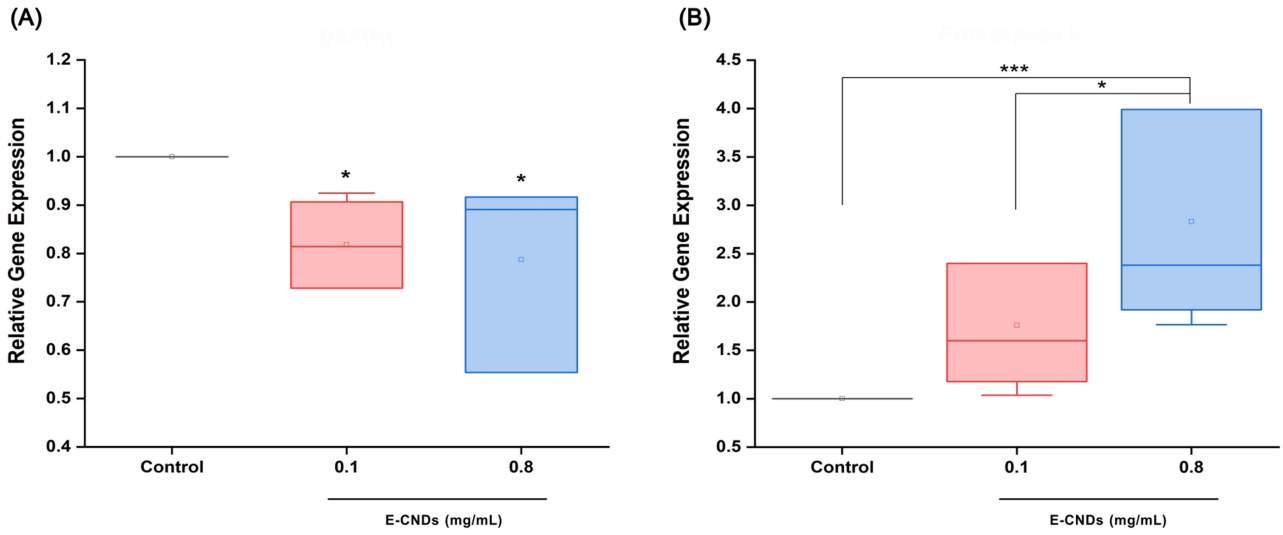

Figure 5 RT-qPCR analysis of G6PDH and procaspase 3 gene expression following treatment with 0.1 and 0.8 mg/mL E-CNDs. Gene expression levels were quantified using the comparative qPCR method ($\Delta\Delta C_T$), with Actin as the housekeeping gene. (**A**) G6PDH expression was significantly downregulated in cells treated with 0.1 mg/mL ($p = 0.0468$) and 0.8 mg/mL ($p = 0.0194$) E-CNDs compared to the control. (**B**) Procaspase 3 expression was significantly upregulated in the 0.8 mg/mL group compared to both the control ($p < 0.0001$) and 0.1 mg/mL group ($p = 0.0108$), while the 0.1 mg/mL vs control comparison was not significant ($p = 0.0801$). Data are presented as mean ± SD from at least three independent experiments. Asterisks indicate statistical significance (*$p < 0.05$, ***$p < 0.001$).

https://doi.org/10.2147/IJN.S544373

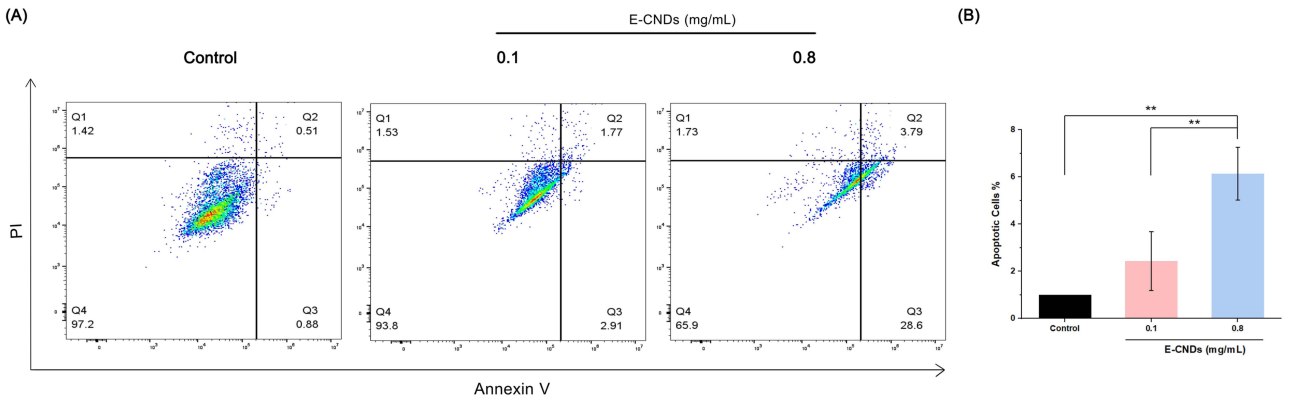

Figure 6 Flow cytometry analysis of Annexin V and propidium iodide (PI) staining following 16 hours of incubation of MDA-MB-231 cells with 0.1 or 0.8 mg/mL E-CNDs. (**A**) Representative flow cytometry plots, shown from left to right: control (cell media), 0.1 mg/mL E-CNDs, and 0.8 mg/mL E-CNDs. Quadrants: Q4 represents viable cells, Q3 indicates early apoptotic cells (Annexin V-positive), Q2 includes late apoptotic or necrotic cells (double-positive for Annexin V and PI), and Q1 represents dead cells (PI-positive). (**B**) Quantification of total apoptotic cells. Apoptotic cell levels in the 0.8 mg/mL group were significantly higher than both the control ($p = 0.0015$) and 0.1 mg/mL group ($p = 0.0079$). Data are presented as mean ± SD from at least three independent experiments. Asterisks indicate statistical significance (**$p < 0.01$).

group and the control. These results suggest that even a relatively small increase in apoptosis can reflect a meaningful cellular response at higher E-CNDs concentrations (Figure 6).

Statistical Analysis

Data are presented as mean ± standard deviation (SD) from three independent experiments. Normal distribution of the data was confirmed using the Kolmogorov–Smirnov test. Statistical significance among groups was assessed by one-way ANOVA followed by Tukey's Honest Significant Difference (HSD) post hoc test. Differences were considered statistically significant at $p < 0.05$, 0.01, and 0.001 (*$p < 0.05$, **$p < 0.01$, ***$p < 0.001$).

Confocal images were analyzed using Fiji (ImageJ). For colocalization analysis, Mander's coefficient was calculated and multiplied by 100 to indicate the percentage of E-CNDs signal overlapping with the mitochondrial signal. Merged TIFF images containing multiple cells were used for analysis. Individual cells were selected, and the combined fluorescence signals from the E-CNDs and MitoTracker channels were defined as the region of interest (ROI). Mander's coefficient (M1) was calculated using JACoP, with Otsu's thresholding method applied beforehand to minimize background noise by automatically determining an optimal cutoff based on the image histogram.

Discussion

CNDs have gained significant attention as low-cost, highly fluorescent nanoparticles for bioimaging applications.[4] First identified during the purification of single-walled carbon nanotubes,[28] CNDs have since been extensively explored for biomedical use, particularly in cancer imaging and therapy.[29–33]

Although CNDs are widely considered biocompatible and low in toxicity,[34,35] their biological safety under different experimental conditions remains a subject of debate. Photodegradation of CNDs has been shown to produce toxic byproducts that compromise cell viability.[21] In addition, concentrations above 0.2 mg/mL have been reported to cause developmental abnormalities in zebrafish embryos, highlighting the potential for dose-dependent toxicity.[22] A recent study in Drosophila melanogaster further showed that cysteamine-functionalized carbon dots induced neurological, developmental, and morphological abnormalities, including abnormal behavior.[23]

E-CNDs predominantly accumulated in the perinuclear region of TNBC cells, with moderate mitochondrial localization and no nuclear penetration. This distribution pattern likely reflects the influence of their negative surface charge, which may have limited mitochondrial uptake,[36] and the lack of nuclear-targeting modifications.[37] Notably, this intracellular localization was accompanied by significant molecular effects. E-CNDs exposure at both 0.1 mg/mL and 0.8 mg/mL concentrations resulted in a marked downregulation of G6PDH expression. As G6PDH is a key regulator of redox homeostasis and

NADPH production,[38,39] its suppression implies that E-CNDs may impair antioxidant defense mechanisms, potentially increasing cellular susceptibility to oxidative stress even in the absence of strong cytotoxic effects.

A significant upregulation of procaspase-3 mRNA expression was also observed following after 16 hours E-CNDs exposure, suggesting activation of proapoptotic signaling. As a central executioner of apoptosis, caspase-3 mediates the dismantling of cellular components via both intrinsic (mitochondrial) and extrinsic (death receptor-mediated) pathways.[40–42]

The moderate mitochondrial localization of E-CNDs may have disrupted mitochondrial integrity, facilitated cytochrome c release, and triggered the intrinsic apoptotic cascade. In parallel, E-CNDs-induced cellular stress could contribute to the activation of death receptors, leading to caspase-8 activation and subsequent cleavage of procaspase-3. Notably, caspase-3 also participates in inflammatory forms of cell death, including pyroptosis, through DFNA5 (GSDME) cleavage, which forms membrane pores and promotes secondary necrosis.[43,44]

The transcriptional shifts in G6PDH and procaspase-3 expression were supported by functional evidence of apoptotic activation. Increased Annexin V/PI staining at both tested concentrations suggests that E-CNDs initiate early and late stages of apoptosis, likely through a combination of oxidative stress and mitochondrial disruption. While Annexin V binding indicates phosphatidylserine externalization during early apoptosis,[45] the rise in PI-positive cells at higher doses may point to progression toward late apoptosis or secondary necrosis.[46]

Taken together, these results demonstrate that although E-CNDs did not reduce cell viability, they induced measurable molecular and apoptotic responses. The scope of this study was to demonstrate that passing a cell viability test alone does not guarantee that an agent is truly biocompatible, and that deeper molecular and functional evaluations are needed for this assumption. For this purpose, we selected E-CNDs, which exhibit moderate colloidal stability, as a representative model and evaluated them in MDA-MB-231 cells, used here as a standard model system. While additional agents and the inclusion of normal or other cancer cell lines would provide broader insight, such comparisons were beyond the scope of the present work. Future studies will extend these evaluations to multiple cell types and in vivo systems to build on the principle established here.

Although gene expression and apoptosis assays suggest a role for oxidative stress, direct quantification of reactive oxygen species (ROS) was not performed, and this will be an important direction for future studies to strengthen the safety assessment of E-CNDs.

Our findings suggest that CCK-8–based measurements of metabolic activity may not fully capture early molecular responses, such as oxidative stress and apoptosis. This highlights the need to supplement standard viability assays with mechanistic analyses to evaluate the biocompatibility of E-CNDs more accurately. While E-CNDs functioned effectively as intracellular imaging agents, they were not biologically inert. Despite no significant reduction in cell viability by CCK-8, E-CNDs exposure led to marked molecular changes—specifically, downregulation of G6PDH, upregulation of procaspase-3, and increased apoptotic cell populations detected by Annexin V/PI staining. Their perinuclear and moderate mitochondrial localization may contribute to these stress responses, particularly at higher concentrations. Overall, these results emphasize that while E-CNDs served here as a representative model, their evaluation underscores the importance of moving beyond surface-level viability assays to account for intracellular effects when assessing biocompatibility.

Conclusion

This study demonstrates that while E-CNDs function as effective intracellular imaging agents in TNBC cells, their biological interactions extend beyond what is captured by standard viability assays. Despite no significant loss of cell viability, E-CNDs modulated oxidative stress and apoptosis pathways, as evidenced by downregulation of G6PDH, upregulation of procaspase-3, and increased apoptotic cell populations. These findings emphasize that viability assays alone are insufficient to define biocompatibility and that molecular- and functional-level analyses are essential for reliable safety assessment. In this work, E-CNDs served as a representative model to illustrate this principle, and future studies involving additional nanomaterials, cell types, and in vivo models will be critical for refining biocompatibility evaluation frameworks.

AI Use Disclosure

The authors confirm that they have read and agree to comply with the Taylor & Francis AI Policy. Generative AI tools were used solely to enhance the clarity, grammar, and fluency of the manuscript. Specifically, ChatGPT (OpenAI, GPT-4, May 2024 version) and Grammarly (version 6.8.263) were used for language editing. The authors entirely developed all scientific content, analysis, and interpretation.

Acknowledgments

We thank Anu Anele for assistance with the synthesis of carbon dots.

Supplementary Materials

Figures S1 and S2 are available in the Supplementary Information.

Funding

This work is supported through NSF award # MCB 2027738 and NIH award # 1R16GM145671.

Disclosure

The authors declare that they have no known competing financial interests or personal relationships that could have appeared to influence the work reported in this paper.

References

1. Tian T, Qiao S, Tannous BA. Nanotechnology-inspired extracellular vesicles theranostics for diagnosis and therapy of central nervous system diseases. *ACS Appl Mater Interfaces*. 2022;15(1):182–199. doi:10.1021/acsami.2c07981
2. Bray F, Laversanne M, Sung H, et al. Global cancer statistics 2022: GLOBOCAN estimates of incidence and mortality worldwide for 36 cancers in 185 countries. *CA Cancer J Clin*. 2024;74(3):229–263. doi:10.3322/CAAC.21834
3. Crosby D, Bhatia S, Brindle KM, et al. Early detection of cancer. *Science*. 2022;375(6586). doi:10.1126/SCIENCE.AAY9040
4. Sharma A, Das J. Small molecules derived carbon dots: synthesis and applications in sensing, catalysis, imaging, and biomedicine. *J Nanobiotechnology*. 2019;17(1):1–24. doi:10.1186/S12951-019-0525-8
5. Shen CL, Liu HR, Lou Q, et al. Recent progress of carbon dots in targeted bioimaging and cancer therapy. *Theranostics*. 2022;12(6):2860. doi:10.7150/THNO.70721
6. Singh G, Kaur H, Sharma A, et al. Carbon based nanodots in early diagnosis of cancer. *Front Chem*. 2021;9. doi:10.3389/fchem.2021.669169
7. Döring A, Ushakova E, Rogach AL. Chiral carbon dots: synthesis, optical properties, and emerging applications. *Light Sci Appl*. 2022;11(1):2047–7538. doi:10.1038/S41377-022-00764-1
8. Jiang K, Uhui Wang Y, Gao X, et al. Facile, quick, and gram-scale synthesis of ultralong-lifetime room-temperature-phosphorescent carbon dots by microwave irradiation. *Angew Chem Int Ed*. 2018;57(21):6216–6220. doi:10.1002/ANIE.201802441
9. Li D, Jing P, Sun L, et al. Near-infrared excitation/emission and multiphoton-induced fluorescence of carbon dots. *Adv Mater*. 2018;30(13):1705913. doi:10.1002/ADMA.201705913
10. Park M, Suk Kim H, Yoon H, et al. Controllable singlet–triplet energy splitting of graphene quantum dots through oxidation: from phosphorescence to TADF. *Adv Mater*. 2020;32(31):2000936. doi:10.1002/ADMA.202000936
11. Chen YY, Jiang WP, Chen HL, et al. Cytotoxicity and cell imaging of six types of carbon nanodots prepared through carbonization and hydrothermal processing of natural plant materials. *RSC Adv*. 2021;11(27):16661–16674. doi:10.1039/D1RA01318A
12. Kim D, Yoo JM, Hwang H, et al. Graphene quantum dots prevent α-synucleinopathy in Parkinson's disease. *Nat Nanotechnol*. 2018;13(9):812. doi:10.1038/S41565-018-0179-Y
13. Liu Y, Liu J, Zhang J, et al. Noninvasive brain tumor imaging using red emissive carbonized polymer dots across the blood-brain barrier. *ACS Omega*. 2018;3(7):7888–7896. doi:10.1021/acsomega.8b01169
14. Bartkowski M, Zhou Y, Nabil Amin Mustafa M, Eustace AJ, Giordani S. CARBON DOTS: bioimaging and anticancer drug delivery. *Chem – a Eur J*. 2024;30(19):e202303982. doi:10.1002/CHEM.202303982
15. Zhang J, Yu SH. Carbon dots: large-scale synthesis, sensing and bioimaging. *Mater Today*. 2016;19(7):382–393. doi:10.1016/J.MATTOD.2015.11.008
16. Liu YY, Sun ZX, Liu J, et al. On the cellular uptake and exocytosis of carbon dots-significant cell type dependence and effects of cell division. *ACS Appl Bio Mater*. 2022;2022:4389. doi:10.1021/acsabm.2c00542
17. Li RS, Gao PF, Zhang HZ, et al. Chiral nanoprobes for targeting and long-term imaging of the Golgi apparatus. *Chem Sci*. 2017;8(10):6829–6835. doi:10.1039/C7SC01316G
18. Liu ML, Chen B, Li CM, Huang CZ. Carbon dots: synthesis, formation mechanism, fluorescence origin and sensing applications. *Green Chem*. 2019;21(3):449–471. doi:10.1039/C8GC02736F
19. Song Y, Zhu S, Yang B. Bioimaging based on fluorescent carbon dots. *RSC Adv*. 2014;4(52):27184–27200. doi:10.1039/C3RA47994C
20. Lim SY, Shen W, Gao Z. Carbon quantum dots and their applications. *Chem Soc Rev*. 2014;44(1):362–381. doi:10.1039/C4CS00269E
21. Liu YY, Yu NY, Di Fang W, et al. Photodegradation of carbon dots cause cytotoxicity. *Nat Commun*. 2021;12(1):1–12. doi:10.1038/s41467-021-21080-z

22. Liu W, Huang G, Su X, et al. Zebrafish: a promising model for evaluating the toxicity of carbon dot-based nanomaterials. *ACS Appl Mater Interfaces*. 2020;12(43):49012–49020. doi:10.1021/acsami.0c17492
23. Pansari P, Sahu S, Alam A, Gupta PK, Mishra M, Durga G. Rational design and in vivo toxicity assessment of multichannel fluorescent carbon dots derived from Withania coagulans in Drosophila melanogaster. *Microchim Acta*. 2025;192(9):1–17. doi:10.1007/s00604-025-07402-8
24. Arvapalli DM, Sheardy AT, Alapati KC, Wei J. High quantum yield fluorescent carbon nanodots for detection of Fe (III) ions and electrochemical study of quenching mechanism. *Talanta*. 2020;209:120538. doi:10.1016/J.TALANTA.2019.120538
25. Shihan MH, Novo SG, Le Marchand SJ, Wang Y, Duncan MK. A simple method for quantitating confocal fluorescent images. *Biochem Biophys Rep*. 2021;25:100916. doi:10.1016/J.BBREP.2021.100916
26. Li Y, Zheng F, Zhang Y, et al. Targeting glucose-6-phosphate dehydrogenase by 6-AN induces ROS-mediated autophagic cell death in breast cancer. *Febs J*. 2023;290(3):763. doi:10.1111/FEBS.16614
27. Ru Y, Waterhouse GI, Lu S. Aggregation in carbon dots. *Aggregate*. 2022;3(6):e296. doi:10.1002/AGT2.296
28. Xu X, Ray R, Gu Y, et al. Electrophoretic analysis and purification of fluorescent single-walled carbon nanotube fragments. *J Am Chem Soc*. 2004;126(40):12736–12737. doi:10.1021/ja040082h
29. Bayda S, Amadio E, Cailotto S, Frión-Herrera Y, Perosa A, Rizzolio F. Carbon dots for cancer nanomedicine: a bright future. *Nanoscale Adv*. 2021;3(18):5183–5221. doi:10.1039/D1NA00036E
30. Mansuriya BD, Altintas Z. Carbon dots: classification, properties, synthesis, characterization, and applications in health care—an updated review (2018–2021). *Nanomaterials*. 2021;11(10):11. doi:10.3390/NANO11102525
31. Nicosia A, Cavallaro G, Costa S, et al. Carbon nanodots for on demand chemophotothermal therapy combination to elicit necroptosis: overcoming apoptosis resistance in breast cancer cell lines. *Cancers*. 2020;12(11):3114. doi:10.3390/CANCERS12113114
32. Miao Y, Wang S, Zhang B, Liu L. Carbon dot-based nanomaterials: a promising future nano-platform for targeting tumor-associated macrophages. *Front Immunol*. 2023;14:1133238. doi:10.3389/FIMMU.2023.1133238
33. Nocito G, Calabrese G, Forte S, et al. Carbon dots as promising tools for cancer diagnosis and therapy. *Cancers*. 2021;13(9):1991. doi:10.3390/CANCERS13091991
34. Boakye-Yiadom KO, Kesse S, Opoku-Damoah Y, et al. Carbon dots: applications in bioimaging and theranostics. *Int J Pharm*. 2019;564:308–317. doi:10.1016/J.IJPHARM.2019.04.055
35. Arvapalli DM, Sheardy AT, Allado K, Chevva H, Yin Z, Wei J. Design of curcumin loaded carbon nanodots delivery system: enhanced bioavailability, release kinetics, and anticancer activity. *ACS Appl Bio Mater*. 2020;3(12):8776–8785. doi:10.1021/acsabm.0c01144
36. Hazra N, Ray R, Banerjee A. Rapid targeting and imaging of mitochondria via carbon dots using an amino acid-based amphiphile as a carrier. *Nanoscale*. 2024;16(20):9827–9835. doi:10.1039/D4NR00665H
37. Havrdová M, Urbančič I, Bartoň Tománková K, Malina L, Štrancar J, Bourlinos AB. Self-targeting of carbon dots into the cell nucleus: diverse mechanisms of toxicity in NIH/3T3 and l929 cells. *Int J Mol Sci*. 2021;22(11):5608. doi:10.3390/IJMS22115608
38. Nakamura M, Magara T, Yoshimitsu M, et al. Blockade of glucose-6-phosphate dehydrogenase induces immunogenic cell death and accelerates immunotherapy. *J Immunother Cancer*. 2024;12(7):e008441. doi:10.1136/JITC-2023-008441
39. Meng Q, Zhang Y, Hao S, et al. Recent findings in the regulation of G6PD and its role in diseases. *Front Pharmacol*. 2022;13:932154. doi:10.3389/FPHAR.2022.932154
40. Zhou M, Liu X, Li Z, Huang Q, Li F, Li CY. Caspase-3 regulates the migration, invasion, and metastasis of colon cancer cells. *Int J Cancer*. 2018;143(4):921. doi:10.1002/IJC.31374
41. Broker LE, Kruyt FAE, Giaccone G. Cell death independent of caspases: a review. *Clin Cancer Res*. 2005;11(9):3155–3162. doi:10.1158/1078-0432.CCR-04-2223
42. Porter AG, Jänicke RU. Emerging roles of caspase-3 in apoptosis. *Cell Death Differ*. 1999;6(2):99–104. doi:10.1038/SJ.CDD.4400476
43. Rogers C, Erkes DA, Nardone A, Aplin AE, Fernandes-Alnemri T, Alnemri ES. Gasdermin pores permeabilize mitochondria to augment caspase-3 activation during apoptosis and inflammasome activation. *Nat Commun*. 2019;10(1):1–17. doi:10.1038/s41467-019-09397-2
44. Rogers C, Fernandes-Alnemri T, Mayes L, Alnemri D, Cingolani G, Alnemri ES. Cleavage of DFNA5 by caspase-3 during apoptosis mediates progression to secondary necrotic/pyroptotic cell death. *Nat Commun*. 2017;8(1):1–14. doi:10.1038/ncomms14128
45. Van Engeland M, Nieland LJW, Ramaekers FCS, Schutte B, Reutelingsperger CPM. Annexin V-affinity assay: a review on an apoptosis detection system based on phosphatidylserine exposure. *Cytometry*. 1998;31(1):1–9. doi:10.1002/(SICI)1097-0320(19980101)31:1<1::AID-CYTO1>3.0.CO;2-R
46. Crowley LC, Scott AP, Marfell BJ, Boughaba JA, Chojnowski G, Waterhouse NJ. Measuring cell death by propidium iodide uptake and flow cytometry. *Cold Spring Harb Protoc*. 2016;2016(7):647–651. doi:10.1101/PDB.PROT087163